Resonant Raman scattering in a zero-gap semiconductor: Interference effects and deformation potentials at the E_1 and $E_1 + \Delta_1$ gaps of HgTe

M. Rösch, R. Atzmüller, G. Schaack, and C. R. Becker
Physikalisches Institut der Universität Würzburg, Am Hubland, D-97074 Würzburg, Germany
(Received 17 January 1994)

The efficiency of resonant Raman scattering by TO and LO phonons in molecular-beam epitaxially grown HgTe is studied for (001), (110), and (111) surfaces with incident photon energies near the E_1 and $E_1+\Delta_1$ band gaps. Absolute values of the Raman scattering efficiency are obtained by means of a sample substitution method and by correcting the experimental data with respect to absorption and reflection losses of the incident and the scattered radiation as well as the different angles of collection inside and outside the sample. We compare our results with calculated resonance profiles assuming uncorrelated electron-hole pairs as intermediate states. Interference effects between dipole-allowed (deformation-potential and electro-optic coupling) and dipole-forbidden scattering by LO phonons in HgTe (001) are used to separate extrinsic (electron-impurity interaction) from intrinsic contributions (Fröhlich intraband coupling) to dipole-forbidden scattering. The optical deformation potentials near the E_1 and $E_1+\Delta_1$ gaps are obtained from TO scattering in HgTe (111) [HgTe (110)] to be $d^5_{1,o}$=−19.9 eV (−21.9 eV) and $d^5_{3,o}$=14.7 eV (13.0 eV). The Faust-Henry coefficient of HgTe is determined.

I. INTRODUCTION

During the last two decades resonant Raman scattering has proved to be a powerful technique to study elementary excitations in semiconductors as well as their interactions. The resonance behavior of the optical phonon Raman efficiency in the vicinity of electronic critical points provides information about both the electron-phonon coupling and the participating intermediate states. Investigations of the Raman efficiency near the interband critical points E_1 and $E_1+\Delta_1$ have been reported for several semiconductors of the diamond and zinc-blende structure.[1–5] These band gaps correspond to transitions along the [111] directions in the Brillouin zone (BZ) where each of the two highest valence bands is nearly parallel to the lowest conduction band (Sec. III A).

Two different mechanisms for electron-phonon interaction are operative in polar materials such as HgTe.[6] The short range deformation-potential coupling leads to an energy shift (two-band process) and a mixing of electronic band states (three-band process). The coupling parameters of this interaction, called "deformation potentials," can be obtained from measurements of the absolute Raman efficiency. The long range Fröhlich interaction causes a change in electronic energies via the macroscopic electric field created by the longitudinal-optical phonon. The Fröhlich Hamiltonian can be expanded into a sum consisting of a two-band term (Fröhlich intraband coupling) as well as a three-band term (electro-optic coupling).[7]

Several contributions to the efficiency of Raman scattering by transverse-optical (TO) and longitudinal-optical (LO) phonons have to be considered near the E_1 and $E_1+\Delta_1$ gaps. Deformation-potential interaction and electro-optic coupling result in the usual selection rules for dipole-allowed scattering by optical phonons, where the electro-optic part affects the LO processes only[8] and can be expressed by the Faust-Henry coefficient.[9] The Fröhlich intraband matrix elements give rise to dipole-forbidden LO scattering if their dependence on the phonon wave vector $\mathbf{q}$ is taken into account.[7] Moreover, the effect of surface electric fields enhancing dipole-forbidden scattering was shown to be important at fields on the order of 10^4 V/cm by Pinczuk and Burstein.[10] An additional, extrinsic dipole-forbidden scattering mechanism involving impurities has been proposed by Gogolin and Rashba.[11] In this case the electron-hole pair is scattered twice: once by the LO phonon via the Fröhlich intraband coupling and once by the electron-impurity interaction. Since the $\mathbf{q}$ conservation is relaxed by the momentum transfer in the impurity scattering, this fourth-order process can be of comparable intensity to intrinsic Fröhlich intraband scattering described in third-order perturbation theory.[12,13]

The study of interference effects between allowed and forbidden scattering by LO phonons enables the separation of intrinsic from extrinsic sources of forbidden scattering.[12] In this way, there has been considerable progress in understanding forbidden Raman scattering in the vicinity of various electronic critical points in many semiconductors.[3,4,12,14–20]

The resonance enhancement of Raman scattering efficiencies near critical points is known to be strongly affected by the electron-hole interaction.[15,21,22] Within the scope of a model which only takes into account uncorrelated electron-hole pairs as intermediate states, excitonic effects at the E_1 and $E_1+\Delta_1$ gaps can be represented by introducing multiplicative factors to the efficiencies of forbidden Raman scattering.[4] In the case of allowed deformation-potential scattering the Raman efficiency can be written in terms of the linear optical sus-

ceptibility and its first derivative.[2] The main effect of the electron-hole interaction usually is included by multiplying the one-electron susceptibility by a phase factor $e^{i\phi}$.[23,24] The investigation of the resonance behavior of forbidden scattering and interference effects thus provides additional information about the role of excitonic interaction in the Raman process.

HgTe plays a particular role within the majority of zinc-blende type materials because it is a zero-gap semiconductor (i.e., a semimetal) with an inverted band structure in the center of the BZ.[25,26] The two highest valence bands in HgTe originate from s- and p-like atomic states, whereas in normal zinc-blende semiconductors such as GaAs, CdTe, etc., they are degenerate components of a p-like state. However, at the E_1 and $E_1+\Delta_1$ gaps ellipsometric measurements demonstrated the similarity of HgTe with other zinc-blende crystals concerning the two optical transition matrix elements which connect the two highest valence bands to the lowest conduction band.[5]

An investigation of TO and LO Raman efficiencies at the E_1 and $E_1+\Delta_1$ band gaps of HgTe was performed by Ingale *et al.*[5] The importance of three-band processes in TO and forbidden LO scattering was found for a p-doped HgTe (111) bulk sample at 90 K, where the forbidden scattering was assigned to a dominance of the impurity mechanism.

Here we present a detailed study of Raman efficiencies in the vicinity of the E_1 and $E_1+\Delta_1$ gaps of three nominally undoped HgTe samples oriented in the (001), (110), and (111) directions. By means of interference effects in scattering by LO phonons, intrinsic and extrinsic sources of forbidden scattering are clearly separated and the role of excitonic effects in the Raman process is studied. The coupling parameters of the electronic states at the E_1 and $E_1+\Delta_1$ gaps to optical phonons, i.e., the deformation potentials $d^5_{1,o}$ and $d^5_{3,o}$,[27] are determined by an analysis of the TO Raman efficiencies in HgTe (110) and HgTe (111), where their signs are derived from the 1LO interference profiles in HgTe (001). A comparison of the Raman polarizabilities of allowed scattering by TO and LO phonons yields the Faust-Henry coefficient for HgTe. In addition, the result of a reflectivity study of HgTe in the energy range of the E_1 and $E_1+\Delta_1$ gaps is presented, which was performed in order to determine the shape of the optical susceptibility at low temperatures.

This paper is arranged as follows. The experimental setup and procedure is given in Sec. II. Section III is devoted to the optical properties of HgTe in the energy range of the E_1 and $E_1+\Delta_1$ gaps, including the results of the reflectivity study. Theoretical expressions for the Raman polarizabilities of the various scattering mechnisms operative near the critical points E_1 and $E_1+\Delta_1$ are reviewed in Sec. IV (written in SI units). In Sec. V we discuss the results of our resonant Raman scattering experiments. Finally the main conclusions are summarized in Sec. VI.

II. EXPERIMENT

The three HgTe samples under investigation with principal faces (001), (110), and (111) were grown on $Cd_{0.96}Zn_{0.04}Te$ and CdTe substrates by molecular-beam epitaxy (MBE)[28] and are nominally undoped. The Raman experiments were performed in a backscattering configuration in a helium bath cryostat at about 1.5 K. A jet-stream dye laser pumped by a continuous-wave (cw) Ar^+ ion laser was used to excite the Raman spectra. The energy regions of the E_1 and $E_1+\Delta_1$ gaps of HgTe were covered by operating the dye laser with Coumarin 510 (2.21–2.45 eV) and Stilbene 3 (2.7–2.98 eV), respectively. Coumarin 510 was pumped by the 457.9 nm line (1.6 W) of the Ar^+ ion laser, while all uv lines (2.8 W) were used to pump Stilbene 3. The laser beam was focused onto the samples with two cylindrical lenses producing a linear focus of about 60 μm width and 3 mm length. Accordingly, the power density was kept below 20 W/cm^2 in order to avoid sample heating. After passing through a 0.5 m triple grating Raman spectrometer the scattered light was analyzed with an optical multichannel detector system.

In Fig. 1 a typical example of our Raman resonance investigations is displayed. The resonant enhancement of the TO, 1LO, and 2LO scattering intensities in HgTe (111) near the E_1 gap (18 107 cm$^{-1}\widehat{=}$ 2.245 eV, Sec. III B) is clearly observed. The one-phonon resonances shown in Fig. 1 will be discussed in detail in Sec. V B.

For a quantitative comparison of experimental and theoretical results, the Raman scattering efficiency $dS/d\Omega$, which is defined as the ratio between the scattered power and the incident power per solid angle $d\Omega$ and scattering length, is a convenient measure of the Raman signal intensity. In order to obtain absolute values for the Raman efficiency we used a sample substitution method,[1] recording the scattered signal of the 522 cm^{-1} 1LO line of silicon as a reference. Each HgTe sample together with the silicon crystal was glued on a sample holder which

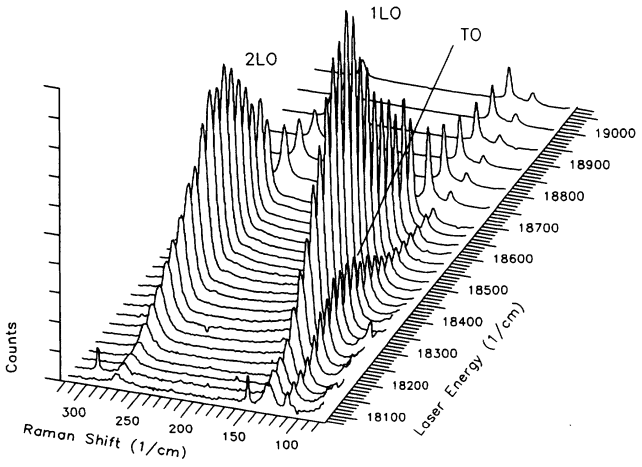

FIG. 1. Resonance behavior of TO, 1LO, and 2LO phonon Raman scattering in a (111)-oriented HgTe sample near the E_1 gap (18107 cm$^{-1}\widehat{=}$2.245 eV). The signal intensities are normalized with respect to the 1LO phonon Raman intensities of Si.

guaranteed that the alternating measurements were performed at reproducible surface positions.

The observed counting rates I for the sample and I^* for the reference *outside* the crystal are related to the Raman scattering efficiency $dS/d\Omega$ *inside* the sample by[1,2]

$$\frac{dS}{d\Omega}(\omega_L) = \frac{K^*(\omega_L,\omega_S)}{K(\omega_L,\omega_S)} \frac{dS^*}{d\Omega}(\omega_L) \frac{I(\omega_L)}{I^*(\omega_L)} , \quad (1)$$

where $dS^*/d\Omega$ is the Raman efficiency of the reference. The functions $K(\omega_L,\omega_S)$ and $K^*(\omega_L,\omega_S)$ are correction factors for sample and reference, respectively, which account for absorption and reflection losses of the incident light with frequency ω_L and the scattered light with frequency ω_S as well as the different angles of collection inside and outside the crystals. In the strong absorption limit, which is valid for HgTe and Si in the energy regions under investigation, the correction factors have the following form:[1]

$$K(\omega_L,\omega_S) = \frac{(1-R_L)(1-R_S)}{(\alpha_L+\alpha_S)\, n_S^2} . \quad (2)$$

Here R_L (R_S) is the reflectivity for the incident (scattered) intensity, α_L (α_S) the corresponding absorption coefficient, and n_S the index of refraction for the scattered radiation.

The 1LO Raman efficiency of Si,[29] as well as its absorption coefficient, reflectivity, and refractive index,[30] were taken from the literature. The corresponding optical constants of HgTe were derived from the complex linear susceptibility $\chi(E)$ obtained by a line shape analysis of the reflectivity spectrum of the (111)-oriented sample at 5 K. Since this procedure requires knowledge of the separate contributions to the function $\chi(E)$, we first consider the optical properties of HgTe in the energy region of the E_1 and $E_1+\Delta_1$ band gaps.

III. OPTICAL PROPERTIES OF HgTe

A. Band structure and optical susceptibility

HgTe is characterized by an inverted band structure in the center of the BZ with respect to the majority of zinc-blende compounds (Fig. 2). In typical direct gap semiconductors such as GaAs, CdTe, etc., the lowest (Γ_6) conduction band originates from an s-like atomic state, while the two highest valence bands (Γ_8), which are degenerate at the Γ point, are of p-like character. Due to relativistic effects the corresponding Γ_6 band in HgTe falls below the Γ_8 state, which is now both the bottom of a conduction band and the top of a valence band.[25,26] Hence due to this zero band gap the II-VI compound HgTe is a semimetal.

However, the irreducible representations of the electronic states at the E_1 and $E_1+\Delta_1$ gaps, which occur on the Λ lines ($\Gamma \rightarrow L$) in the BZ where the $\Lambda_{4,5}$ ($v1$) and Λ_6 ($v2$) valence bands (notation of Ref. 31) are nearly parallel to the Λ_6 conduction band (c), are the same as in typical zinc-blende semiconductors. Note that for reasons of symmetry there exist eight E_1 and $E_1+\Delta_1$ gaps within the BZ, where the gaps along opposite valleys are

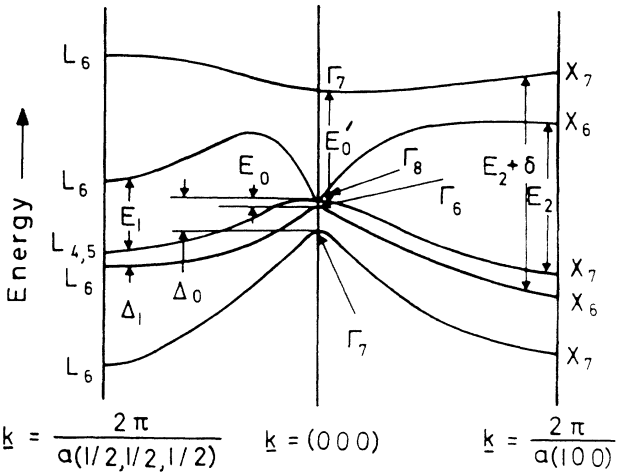

FIG. 2. Schematic band structure of HgTe in the principal symmetry directions Λ ([111]) and Δ ([100]), illustrating the positions of several observed interband transitions (from Ref. 25).

Kramers degenerate. The E_1 and $E_1+\Delta_1$ band gaps can be considered as two dimensional (2D) or M_1-type critical points since here the reduced joint-density-of-states mass $\mu_{\|}$ along Λ is very large in comparison with the transverse mass $\mu_\perp$.

The contributions of interband transitions at the E_1 and $E_1+\Delta_1$ critical points to the linear susceptibility of HgTe are given as a function of the energy E by[1,2,32]

$$\chi^{E_1}(E) = -\frac{8e^2\mu_\perp^{E_1}\,|\langle c|\hat{\mathbf{e}}\cdot\mathbf{p}|v1\rangle|^2}{\sqrt{3}\pi a_0\varepsilon_0 m_0^2 E^2} \ln(1-x_{E_1}^2)\, e^{i\phi_1} \quad (3)$$

and

$$\chi^{E_1+\Delta_1}(E) = -\frac{8e^2\mu_\perp^{E_1+\Delta_1}\,|\langle c|\hat{\mathbf{e}}\cdot\mathbf{p}|v2\rangle|^2}{\sqrt{3}\pi a_0\varepsilon_0 m_0^2 E^2} \times \ln(1-x_{E_1+\Delta_1}^2)\, e^{i\phi_2} . \quad (4)$$

The quantities x_{E_1} and $x_{E_1+\Delta_1}$ in Eqs. (3) and (4) are reduced energies defined as $x_{E_1} = E/(E_1 - i\Gamma_1)$ and $x_{E_1+\Delta_1} = E/(E_1+\Delta_1 - i\Gamma_2)$, respectively, where Γ_1 and Γ_2 take into account the broadening of the corresponding gaps. Here $\mu_\perp^{E_1} = [(1/m_{\perp e})+(1/m_{\perp h1})]^{-1}$ and $\mu_\perp^{E_1+\Delta_1} = [(1/m_{\perp e})+(1/m_{\perp h2})]^{-1}$ are reduced joint-density-of-states masses, where $m_{\perp e}$ ($m_{\perp h1,h2}$) is the mass of the conduction band c (valence band $v1$, $v2$) in the directions perpendicular to Λ. The phase angles ϕ_1 and ϕ_2 describe the character of the 2D critical points ($\phi = 0$ for a 2D minimum, $\phi = \pi/2$ for a 2D saddle point) as well as excitonic effects within the Koster-Slater approximation.[23] The importance of the electron-hole interaction at M_1-type critical points has been emphasized by several authors.[33–35] The two optical transition matrix elements $\langle c|\hat{\mathbf{e}}\cdot\mathbf{p}|v1\rangle$ and $\langle c|\hat{\mathbf{e}}\cdot\mathbf{p}|v2\rangle$ correspond to transitions at the E_1 and $E_1+\Delta_1$ energy gaps, respectively, for a polarization of the light $\hat{\mathbf{e}}$ and an electron momentum $\mathbf{p}$. In Eqs. (3) and (4) a_0 is the lattice constant, ε_0 the vacuum permittivity, e the electron charge,

and m_0 the free electron mass.

Within $\mathbf{k}\cdot\mathbf{p}$ theory the reduced masses $\mu_\perp^{E_1}$ and $\mu_\perp^{E_1+\Delta_1}$ are approximately given by $\mu_\perp^{E_1} \approx m_0^2 (E_1 + \Delta_1/3)/3\overline{P}^2$ and $\mu_\perp^{E_1+\Delta_1} \approx m_0^2 (E_1 + 2\Delta_1/3)/3\overline{P}^2$,[36] where the Kane matrix element $\overline{P}$ is defined as $\overline{P} := i\langle\overline{X}|p_x|S\rangle := i\langle\overline{Y}|p_y|S\rangle$. The vectors $\overline{X}$ and $\overline{Y}$ are chosen to be perpendicular to the direction Λ. Since $|\langle c|\hat{\mathbf{e}}\cdot\mathbf{p}|v1\rangle|^2 = |\langle c|\hat{\mathbf{e}}\cdot\mathbf{p}|v2\rangle|^2 = \overline{P}^2/2$,[36] Eqs. (3) and (4) can be rewritten in a simplified form as[3]

$$\chi^{E_1}(E) = -\frac{A^{E_1}}{E^2}(E_1 + \Delta_1/3)\ln(1 - x_{E_1}^2)\, e^{i\phi_1} \qquad (5)$$

and

$$\chi^{E_1+\Delta_1}(E) = -\frac{A^{E_1+\Delta_1}}{E^2}(E_1 + 2\Delta_1/3) \times \ln(1 - x_{E_1+\Delta_1}^2)\, e^{i\phi_2}\,, \qquad (6)$$

introducing the real amplitudes $A^{E_1} \approx A^{E_1+\Delta_1} \approx 4\sqrt{3}e^2/9\pi\varepsilon_0 a_0 = 6.874$ eV. These amplitudes are treated as adjustable parameters when determining the shape of the optical susceptibility from experiment.

B. Reflectivity measurement and evaluation

The dispersion of the optical susceptibility $\chi(E)$ in the vicinity of the E_1 and $E_1+\Delta_1$ gaps must be known exactly to determine absolute Raman efficiencies by the sample substitution method [Eq. (1)]. Ellipsometric measurements on HgTe at room temperature have been performed by Viña *et al.*[24] and Ingale *et al.*[5] However, since the critical point energies and linewidths strongly depend on sample temperature, knowledge of the optical susceptibility in the temperature range of the Raman measurements is necessary.

In order to obtain the frequency dependence of the optical susceptibility, the reflectivity of HgTe (111) in the energy range from 1.1 to 3.5 eV was recorded at 5 K. The part of this spectrum between 2.1 and 3.1 eV is shown by the solid line in Fig. 3(a). The structure with two distinct peaks due to the E_1 and $E_1+\Delta_1$ critical points [noted in Fig. 3(a)] is excellently described by a theory [dashed line in Fig. 3(a)] based on the optical susceptibilities χ^{E_1} and $\chi^{E_1+\Delta_1}$ [Eqs. (5) and (6)], and additional contributions due to the E_0 and E_2 gaps.[2,23]

We determined the parameters necessary for an analytical description of the optical susceptibility $\chi(E)$ in the energy range of the E_1 and $E_1+\Delta_1$ critical points (transition energies, linewidths, amplitudes, phase angles) by a line shape analysis of the measured reflectivity spectrum. A Kramers-Kronig transformation was performed after every step of the fit procedure to yield the real part of the underlying $\chi(E)$ from the corresponding imaginary part. Since Kramers-Kronig analysis requires knowledge of the reflectivity over a wide energy range, additional data below 1.1 eV and above 3.5 eV were taken from the literature.[24,37] The fitted parameters are $E_1 = 2.245$ eV, $\Gamma_1 = 0.015$ eV, $A^{E_1} = 5.639$ eV, $\phi_1 = 1.19$ rad and $E_1+\Delta_1 = 2.877$ eV, $\Gamma_2 = 0.025$ eV, $A^{E_1+\Delta_1} = 6.389$ eV, $\phi_2 = 1.23$ rad. The values of the phase angles imply that the E_1 and $E_1+\Delta_1$ gaps are affected by the excitonic interaction, since these critical points are described as 2D minima ($\phi = 0$) in a one-particle model.[24] From the re-

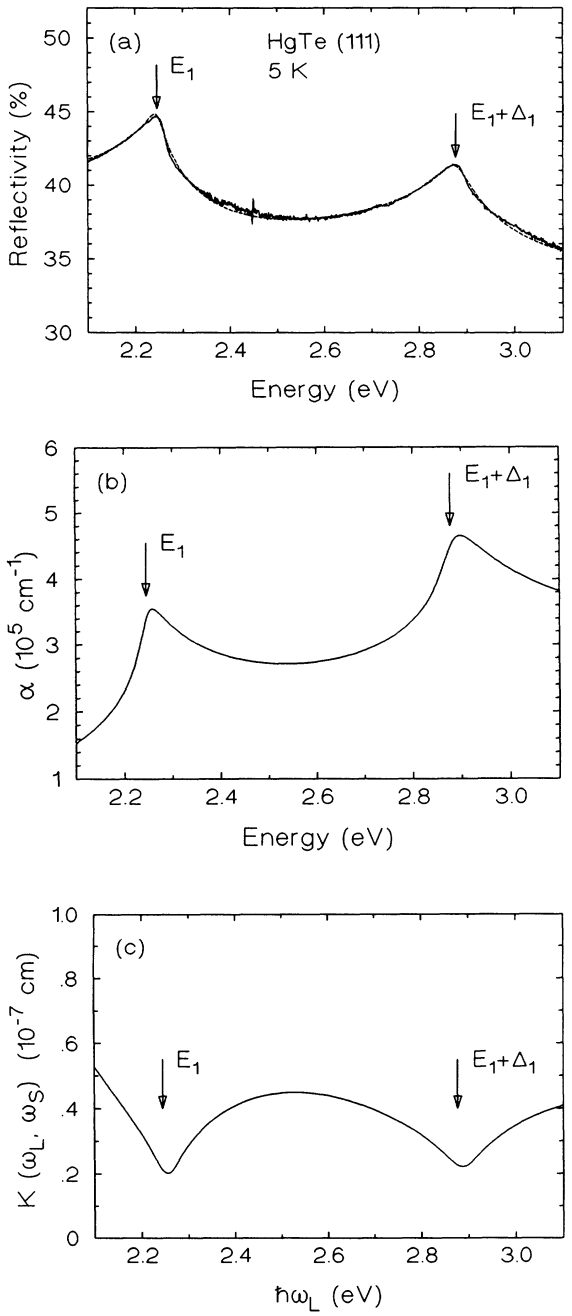

FIG. 3. (a) Experimental (solid line) and calculated reflectivity spectrum (dashed line) of HgTe (111) at 5 K in the energy range between 2.1 and 3.1 eV. The arrows at E_1 and $E_1+\Delta_1$ mark the transition energies obtained from the fit. A Kramers-Kronig analysis of the reflectivity spectrum yielded the complex optical susceptibility of HgTe. (b) Absorption coefficient α and (c) LO correction factor $K(\omega_L, \omega_S)$ for HgTe, derived from the optical susceptibility.

sulting optical susceptibility, the absorption coefficient α [Fig. 3(b)] and thus the correction factor $K(\omega_L,\omega_S)$ [Fig. 3(c)] for HgTe was derived.

IV. THEORY

For one-phonon scattering, the Raman efficiency can be expressed as a function of the Raman tensor $\overleftrightarrow{R}$ in the following form:[12]

$$\frac{dS}{d\Omega}=\frac{\omega_S^3\omega_L}{c^4}\frac{\hbar}{2V_cM^*\Omega_{\rm ph}}\frac{n_S}{n_L}|\hat{\mathbf{e}}_S\cdot\overleftrightarrow{R}\cdot\hat{\mathbf{e}}_L|^2[n(\Omega_{\rm ph})+1]\,, \tag{7}$$

where $\hat{\mathbf{e}}_L$ ($\hat{\mathbf{e}}_S$) is the incident (scattered) photon polarization vector, n_L (n_S) the corresponding index of refraction, $n(\Omega_{\rm ph})$ the Bose occupation factor of an optical phonon with frequency $\Omega_{\rm ph}$, $V_c=a_0^3/4$ the volume and $M^*=(1/M_{\rm Hg}+1/M_{\rm Te})^{-1}$ the reduced mass of the primitive unit cell, and c the speed of light in vacuum. The independent components of the Raman tensor $\overleftrightarrow{R}$, called Raman polarizabilities and labeled a, are related to the transition amplitude W_{fi} [Eq. (12) in Ref. 12] between an initial state $|i,\hat{\mathbf{e}}_L\rangle$ and a final state $|f,\hat{\mathbf{e}}_S\rangle$ by[4,38]

$$a=\frac{n_Ln_S}{2\pi}\frac{V_c}{\bar{u}_0}\frac{1}{\hbar\omega_L}W_{fi}(\hat{\mathbf{e}}_S,\hat{\mathbf{e}}_L)\,. \tag{8}$$

Here $\bar{u}_0=(\hbar V_c/2VM^*\Omega_{\rm ph})$ is the zero-point amplitude of the optical phonon, where V is the crystal volume. Theoretical expressions for the scattering amplitudes W_{fi} can be derived in time-dependent perturbation theory.[38]

Different mechanisms of scattering by TO and LO phonons resonant near the E_1 and $E_1+\Delta_1$ gaps must be taken into account. The corresponding Raman polarizabilities based on the assumption of free-electron–hole pairs as intermediate states have been treated in detail by Richter *et al.*[39] and Kauschke *et al.*[4]

A. Allowed scattering by TO and LO phonons

Dipole-allowed scattering by TO phonons arises from deformation-potential interaction only, including two-band processes as well as three-band processes. An additional contribution to dipole-allowed scattering by LO phonons is due to Fröhlich interband (electro-optic) coupling.

The Raman tensor for deformation-potential (DP) scattering can be derived in third-order perturbation theory. For backscattering at a (001) face it has the form[2,39]

$$\overleftrightarrow{R}_{{\rm DP},z}=\begin{pmatrix}0 & a_{\rm DP} & 0\\ a_{\rm DP} & 0 & 0\\ 0 & 0 & 0\end{pmatrix}. \tag{9}$$

The contributions of the DP process to backscattering at (110) and (111) surfaces will be discussed in Sec. IV C. The Raman polarizability $a_{\rm DP}$ in the vicinity of the E_1 and $E_1+\Delta_1$ gaps can be written as a function of the optical susceptibilities χ^{E_1} and $\chi^{E_1+\Delta_1}$ [Eqs. (5) and (6)]:[2]

$$a_{\rm DP}=\frac{1}{4\pi}\frac{a_0^2}{4\sqrt{6}}\left[-\frac{1}{2\sqrt{2}}d_{1,o}^5\left(\frac{d\chi^{E_1}}{dE_1}+\frac{d\chi^{E_1+\Delta_1}}{d(E_1+\Delta_1)}\right)+2\,d_{3,o}^5\,\frac{\chi^{E_1}-\chi^{E_1+\Delta_1}}{\Delta_1}+B\right]. \tag{10}$$

The derivatives on the right-hand side of Eq. (10) are given by (for $E_g=E_1$ and $E_g=E_1+\Delta_1$, respectively)

$$\frac{d\chi^{E_g}}{dE_g}=-\frac{E}{E_g}\frac{d\chi^{E_g}}{dE}-\frac{\xi}{E}\chi^{E_g}\,, \tag{11}$$

where the parameter ξ describes the variation of the transverse reduced joint-density-of-states mass $\mu_\perp^{E_g}$ with phonon perturbation. If the phonon does not affect the electron band, $\mu_\perp^{E_g}$ is independent of E_g corresponding to the case $\xi=2$. A linear dependence of $\mu_\perp^{E_g}$ on E_g is equivalent to $\xi=1$.[2]

The Raman polarizability $a_{\rm DP}$ [Eq. (10)] consists of a two-band contribution arising from the phonon-induced modulation of the gaps (deformation potential $d_{1,o}^5$),[40] a three-band term describing the coupling of the $\Lambda_{4,5}$ and Λ_6 valence bands (deformation potential $d_{3,o}^5$), and a real constant B representing the contribution of interband transitions far removed from the E_1 and $E_1+\Delta_1$ gaps. Equation (10) holds for the adiabatic approximation only (i.e., the limit where the phonon energies can be neglected with respect to $|\hbar\omega_L-E_1+i\Gamma_1|$ and $|\hbar\omega_L-E_1-\Delta_1+i\Gamma_2|$), otherwise the derivatives in the two-band term have to be replaced by the finite differences of the susceptibilities at $E=\hbar\omega_L$ and $E=\hbar\omega_S$. However, for $\hbar\Omega_{\rm ph}\approx\Gamma_{1,2}$ (as is the case for the E_1 and $E_1+\Delta_1$ gaps of HgTe at 1.5 K) the error using Eq. (10) was shown to be less than 5%.[3]

The two-band terms give rise to sharp resonance maxima near $E_1+\hbar\Omega_{\rm ph}/2$ and $E_1+\Delta_1+\hbar\Omega_{\rm ph}/2$ (for $\hbar\Omega_{\rm ph}\le\Gamma_1,\Gamma_2$); the three-band contribution produces mainly a broad resonance between E_1 and $E_1+\Delta_1$. The sign of $a_{\rm DP}$ is determined by the signs of the deformation potentials ($d_{1,o}^5<0, d_{3,o}^5>0$).[4,27] Figure 4 shows the effect of the three-band term on the resonance profile of $|a_{\rm DP}|^2$. The curves were calculated with Eq. (10) for three different values of the ratio $d_{3,o}^5/d_{1,o}^5$, using parameters appropriate to the E_1 and $E_1+\Delta_1$ gaps of HgTe.

The expression for the three-band term in Eq. (10) is correct only under the assumption of an approximate equality of the two optical transition matrix elements in Eqs. (3) and (4).[1] Consequently, Ingale *et al.*[5] pointed out that because of its inverted band structure the validity of this requirement has to be verified in the case of HgTe. Following Ref. 5, the amplitudes A^{E_1} and $A^{E_1+\Delta_1}$ obtained from the reflectivity measurement were analyzed with regard to the two transition matrix elements between the states forming the E_1 and $E_1+\Delta_1$ gaps to check the applicability of Eq. (10) in our case. Using Eqs. (3) and (4) and inserting the reduced joint-density-of-states masses from $\mathbf{k}\cdot\mathbf{p}$ theory (Sec. III A), the ratio was found to be $|\langle c|\hat{\mathbf{e}}\cdot\mathbf{p}|v1\rangle|^2/|\langle c|\hat{\mathbf{e}}\cdot\mathbf{p}|v2\rangle|^2=0.88$, a

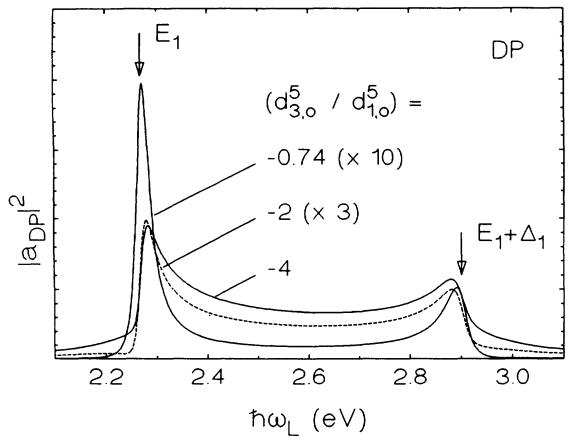

FIG. 4. Squared Raman polarizability of deformation-potential (DP) scattering, calculated with Eq. (10) using parameters appropriate to the E_1 and $E_1+\Delta_1$ gaps of HgTe for three different values of the ratio $d^5_{3,o}/d^5_{1,o}$ (−0.74, −2, and −4) with fixed $d^5_{1,o}$. The value $d^5_{3,o}/d^5_{1,o}=-0.74$ corresponds to the result obtained for HgTe (111) in this article.

result similar to that of Ref. 5. Thus our experiment likewise shows the applicability of Eq. (10) to describe DP scattering in HgTe.

Deformation-potential scattering by LO phonons[8] is accompanied by electro-optic (EO) scattering due to their macroscopic electric field $E_{\rm LO}$, since the electro-optic and deformation-potential interactions produce Raman tensor contributions of the same symmetry.[2–4] The ratio of $a_{\rm LO}$ (EO and DP contribution to scattering by LO phonons) to $a_{\rm TO}$ (pure DP scattering by TO phonons) is determined by the complex Faust-Henry coefficient C,[2,9]

$$\frac{a_{\rm LO}}{a_{\rm TO}}=1-\frac{\Omega^2_{\rm LO}-\Omega^2_{\rm TO}}{C\,\Omega^2_{\rm TO}}\,, \tag{12}$$

where $\Omega_{\rm LO}$ and $\Omega_{\rm TO}$ denote the frequencies of LO and TO phonons, respectively. The dimensionless parameter C is given by[2]

$$C=\frac{e^*(\partial\chi/\partial u)}{M^*\Omega^2_{\rm TO}(\partial\chi/\partial E_{\rm LO})} \tag{13}$$

and is a measure of the relative strength of the DP coupling $[(\partial\chi/\partial u)]$ to the EO mechanism $[(\partial\chi/\partial E_{\rm LO})]$, where e^* is the effective charge associated with the optical phonons. The Faust-Henry coefficient can be either positive or negative, leading to weakened or enhanced scattering intensities for the LO phonon compared with the TO phonon.[2]

B. Forbidden scattering by LO phonons

Scattering mechanisms violating the usual dipole selection rules [Eq. (9)] are called forbidden since the contributions of electrons and holes cancel exactly if the phonon wave vector $\mathbf{q}$ is taken to be zero (dipole approximation). Due to the finiteness of the wave vector $\mathbf{q}$ these processes become "allowed" in a backscattering configuration and can produce higher scattering efficiencies than the dipole-allowed terms in the proximity of critical points.[2]

Intrinsic forbidden scattering by LO phonons is produced by Fröhlich intraband (F) coupling[41] and, in addition, can be induced by electric fields due to space-charge layers if the scattering volume is close to the sample surface.[10] As in the allowed case, intrinsic forbidden scattering obeys crystal-momentum conservation, i.e., the phonon wave vector is given by $\mathbf{q}=\mathbf{k}_L-\mathbf{k}_S$, where $\mathbf{k}_L$ ($\mathbf{k}_S$) is the wave vector of the incident (scattered) photon.

The Raman tensor of $\mathbf{q}$-dependent Fröhlich intraband scattering (two-band process) has been calculated in third-order perturbation theory. Near the E_1 gap it has the form[4,42]

$$\begin{aligned}\overleftrightarrow{R}_F=&-i\frac{\sqrt{3}f}{4\pi a_0}\frac{1}{\omega_L(\omega_L\omega_S)^{1/2}}\frac{1}{4\pi\varepsilon_0}\left(\frac{e}{m_0}\right)^2\frac{V_c}{V^{1/2}\bar{u}_0}\,\overline{P}^2\\&\times\frac{C_F}{(\hbar\Omega_{\rm LO})^2}(s_e-s_{h1})[2+(\alpha+\beta)(\ln\beta-\ln\alpha)]\\&\times\hat{\mathbf{e}}_{\rm LO}\cdot\mathbf{q}\sum_{l=1}^{4}\frac{2}{q^2}(\mathbf{q}\cdot\overleftrightarrow{T}_l\cdot\mathbf{q})\,\overleftrightarrow{T}_l\,,\end{aligned} \tag{14a}$$

$$\alpha=\frac{\hbar\omega_L-E_1+i\Gamma_1}{\hbar\Omega_{\rm LO}}\,,\qquad \beta=\alpha-1\,. \tag{14b}$$

In Eq. (14a) C_F represents the Fröhlich interaction constant: $C_F=e\,[\hbar\Omega_{\rm LO}(1/\varepsilon_\infty-1/\varepsilon_S)/2\varepsilon_0]^{1/2}$ [written in terms of the static (ε_S) and high frequency (ε_∞) dielectric constants], $s_{e(h1)}$ represents the reduced mass: $s_{e(h1)}=m_{\perp e(h1)}/(m_{\perp e}+m_{\perp h1})$, and f the fraction of the distance in the BZ between Γ and L where the $\Lambda_{4,5}$ and Λ_6 valence bands are nearly parallel to the Λ_6 conduction band [f is estimated to be 1/2 in HgTe (Ref. 37)]. The unit vector $\hat{\mathbf{e}}_{\rm LO}$ characterizes the relative atomic displacements in the LO phonon mode measured in Raman scattering and is choosen here to be antiparallel to the direction of $\mathbf{q}$. The $\overleftrightarrow{T}_l$ matrices describe projection operators $1-|\hat{\mathbf{e}}_l\rangle\langle\hat{\mathbf{e}}_l|$ onto the $l=1,2,3,4$ valleys (where the $\hat{\mathbf{e}}_l$ vectors are unit vectors pointing in the direction of the lth valley) arising from the fact that only the matrix elements $\overline{P}=i\langle\overline{X}|p_x|S\rangle=i\langle\overline{Y}|p_y|S\rangle$ contribute to optical transitions at the E_1 gap,

$$\begin{aligned}&\overleftrightarrow{T}_1=\frac{1}{6}\begin{pmatrix}2&-1&-1\\-1&2&-1\\-1&-1&2\end{pmatrix},\quad \overleftrightarrow{T}_2=\frac{1}{6}\begin{pmatrix}2&1&1\\1&2&-1\\1&-1&2\end{pmatrix},\\&\overleftrightarrow{T}_3=\frac{1}{6}\begin{pmatrix}2&1&-1\\1&2&1\\-1&1&2\end{pmatrix},\quad \overleftrightarrow{T}_4=\frac{1}{6}\begin{pmatrix}2&-1&1\\-1&2&-1\\1&1&2\end{pmatrix}.\end{aligned} \tag{15}$$

An expression similar to Eq. (14a) holds for the $E_1+\Delta_1$ gap, with $E_1+i\Gamma_1$ replaced by $E_1+\Delta_1+i\Gamma_2$ in the quantity α and the corresponding reduced mass s_{h2} inserted.

For backscattering at a (001) face $\overleftrightarrow{R}_F$ is diagonal, since the sum in Eq. (14a) becomes $\frac{8}{9}\overleftrightarrow{1}$:[4]

$$\overleftrightarrow{R}_F = \begin{pmatrix} a_F & 0 & 0 \\ 0 & a_F & 0 \\ 0 & 0 & a_F \end{pmatrix}, \tag{16}$$

where the Raman polarizability a_F is given by

$$a_F = i\frac{2\sqrt{3}f}{9\pi a_0}\frac{1}{\omega_L(\omega_L\omega_S)^{1/2}}\frac{1}{4\pi\varepsilon_0}\left(\frac{e}{m_0}\right)^2\frac{V_c}{V^{1/2}\overline{u}_0}\overline{P}^2 \times \frac{C_F}{(\hbar\Omega_{\mathrm{LO}})^2}(s_e - s_{h1})\,q \times [2 + (\alpha+\beta)(\ln\beta - \ln\alpha)]. \tag{17}$$

The Raman tensors for backscattering at (110) and (111) faces are derived by a transformation of the $\overleftrightarrow{T}_l$ matrices into coordinate systems with corresponding symmetries. In the case of a (110) surface one obtains

$$\overleftrightarrow{R}_F = a_F \begin{pmatrix} 3/4 & 0 & 0 \\ 0 & 1 & 0 \\ 0 & 0 & 5/4 \end{pmatrix}, \tag{18}$$

and for a (111) surface we find

$$\overleftrightarrow{R}_F = a_F \begin{pmatrix} 5/6 & 0 & 0 \\ 0 & 5/6 & 0 \\ 0 & 0 & 4/3 \end{pmatrix}. \tag{19}$$

Figure 5 displays the resonance shape of $|a_F|^2$ in the vicinity of the E_1 gap of HgTe, calculated with Eq. (17) for different values of the damping constant Γ_1 and the material parameters of HgTe. The squared Raman polarizability $|a_F|^2$ produces maxima of nearly equal size at

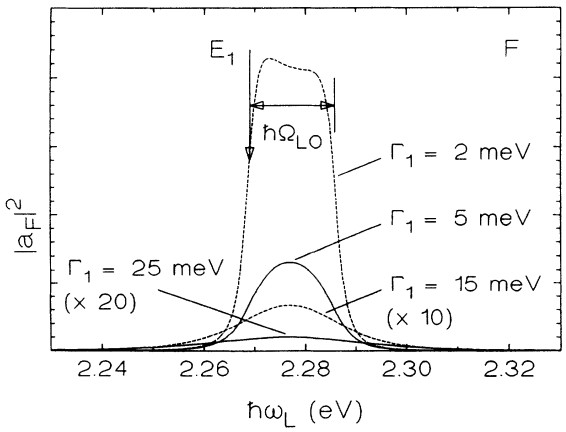

FIG. 5. Squared Raman polarizability of Fröhlich intraband (F) scattering, calculated with Eq. (17) using parameters appropriate to HgTe for four different broadenings of the E_1 gap (Γ_1 = 2, 5, 15, and 25 meV). The latter two values correspond to the results obtained for HgTe at the E_1 and $E_1 + \Delta_1$ gaps, respectively.

E_1 (incoming resonance) and $E_1 + \hbar\Omega_{\mathrm{LO}}$ (outgoing resonance). However, for $\Gamma_1 > 2$ meV the two resonances cannot be separated and only one resonance maximum appears at $E_1 + \hbar\Omega_{\mathrm{LO}}/2$. The sign of a_F depends on the difference $m_{\perp e} - m_{\perp h1(h2)} < 0$ and on C_F.[4]

Dipole-forbidden Raman scattering by LO phonons can be enhanced if electric fields due to space-charge layers near the sample surface exist. The importance of this process was shown by Pinczuk and Burstein[10] for surface electric fields of the order of 10^4 V/cm. The surface-field-induced (E) mechanism should be particularly noticeable in the vicinity of the E_1 and $E_1 + \Delta_1$ gaps since in this energy region the penetration depth of light (ca. 200 Å for HgTe) is of the same order of magnitude as the thickness of space-charge layers. The corresponding Raman tensor for backscattering at a (001) face is diagonal, as in the case of Fröhlich intraband scattering.[3,4,39] Since real and imaginary parts of the Raman polarizabilities of the E mechanism and the F mechanism show a similar dependence on laser energy and because the same selection rules are valid,[4] the two processes cannot be distinguished without applying an external electric field. Consequently, we assume intrinsic forbidden scattering to be primarily F induced and take E scattering into account by multiplying a_F with a constant factor.

An additional extrinsic dipole-forbidden scattering mechanism proposed by Gogolin and Rashba[11] involving electron-impurity interaction was shown to be operative near the E_1 gap in InSb (Ref. 3) and in the vicinity of the E_1 and $E_1 + \Delta_1$ gaps of GaSb.[4] In this case the electron-hole pair is scattered twice, once due to the Fröhlich intraband interaction and once elastically by the screened Coulomb potential of an ionized impurity. Although impurity-induced scattering is a process calculated in fourth-order perturbation theory, its magnitude can be comparable to intrinsic F-induced scattering.[13] This is mainly based on the fact that due to the repeated interaction the momentum conservation $\mathbf{q} = \mathbf{k}_L - \mathbf{k}_S$ is relaxed and LO phonons of an extended area of the BZ participate in Raman scattering: the difference between the phonon wave vector $\mathbf{q}$ and the small optical wave vector $\mathbf{k}_L - \mathbf{k}_S$ is compensated by the impurity. In particular the contribution of phonons with large $\mathbf{q}$ vectors strongly increases the scattering efficiency of this mechanism because of the $\mathbf{q}$ dependence of the Fröhlich intraband process. Furthermore, processes relaxing the wave vector conservation enable double-resonance effects[43] producing an additional enhancement of the Raman efficiency.

The squared Raman polarizability $|a_{\mathrm{FI}}|^2$ of the impurity-induced (FI) mechanism in the vicinity of the E_1 ($E_1 + \Delta_1$) gap has been calculated by Kauschke *et al.*[4] For backscattering at a (001) face the Raman tensor of the FI process is again diagonal. The Raman resonance shape of the impurity-induced mechanism near the E_1 ($E_1 + \Delta_1$) critical point consists of an incoming resonance at E_1 ($E_1 + \Delta_1$) and an outgoing resonance at $E_1 + \hbar\Omega_{\mathrm{LO}}$ ($E_1 + \Delta_1 + \hbar\Omega_{\mathrm{LO}}$), where the outgoing one is strongly enhanced by double-resonance effects.[4] Therefore, with increasing broadening of the gap only one maximum of the impurity-induced scattering occurs at $E_1 + \hbar\Omega_{\mathrm{LO}}/2$ ($E_1 + \Delta_1 + \hbar\Omega_{\mathrm{LO}}/2$).

C. Interference effects in scattering by LO phonons

Since the long range Fröhlich interaction and the short range deformation-potential coupling are strictly additive,[6] interference effects between allowed and forbidden scattering by LO phonons occur for suitable geometries. Deformation-potential and Fröhlich intraband scattering interfere coherently because both are intrinsic processes with the **q** vector of the final state (LO phonon) fixed by momentum conservation. Thus, when calculating the Raman efficiency of the interference between the two mechanisms the Raman tensors for allowed and F-induced forbidden scattering have to be added before squaring. In contrast, the tensor for impurity-induced scattering must be added to the intrinsic contribution after squaring, since the extrinsic mechanism results in a broad distribution of final states with different **q** vectors.[12] In this paper we represent $a_{\rm FI}$ by the same expression as in Eq. (17), but shifted by $\hbar\Omega_{\rm LO}/2$ to higher energies. The two main effects of impurity-induced scattering, the shifted resonance maximum and its incoherent character, can be taken into account in this way.

The selection rules for the described scattering mechanisms in the energy range of the E_1 and $E_1+\Delta_1$ gaps for backscattering at (001), (110), and (111) faces are summarized in Table I. The notation of the crystal axes for the (001) surface and the definition of the unit cell [Hg at the origin and Te at $a_0/4\,(1,1,1)$] refers to that of Fig. 1 in Ref. 12. Such a convention is necessary because the [110] and $[\bar{1}10]$ directions are physically inequivalent in zinc-blende compounds and the labeling depends on the positions of cations and anions in the coordinate system.[12] In the case of backscattering at (110) and (111) faces it is convenient to choose coordinate systems with corresponding symmetries. The scattering geometries are written in the Porto notation defined as $\hat{\mathbf{k}}_L(\hat{\mathbf{e}}_L,\hat{\mathbf{e}}_S)\hat{\mathbf{k}}_S$.

For backscattering at a (001) surface, in the $\bar{z}(x',x')z$ configuration a destructive interference between allowed and forbidden scattering by LO phonons at the E_1 gap and a constructive interference at the $E_1+\Delta_1$ gap is expected: the sign of the three-band contribution to $a_{\rm DP}$ changes between E_1 and $E_1+\Delta_1$, while real and imaginary parts of a_F have the same sign at E_1 and $E_1+\Delta_1$.[4] In the $\bar{z}(y',y')z$ geometry the interference is constructive near the E_1 gap and becomes destructive in the vicinity of the $E_1+\Delta_1$ gap. Thus, if the directions of the physically inequivalent axes x' ([110]) and y' ($[\bar{1}10]$) are known on a (001) surface, the signs of the deformation potentials $d^5_{1,o}$ and $d^5_{3,o}$ can be determined.[3] If the impurity-induced mechanism dominates, the $\bar{z}(x',x')z$ and $\bar{z}(y',y')z$ configurations should give nearly the same result, whereas a different behavior is expected if the intrinsic mechanisms play an important role.

TABLE I. Selection rules of dipole-allowed and dipole-forbidden contributions to backscattering at (001), (110), and (111) surfaces of zinc-blende crystals in the vicinity of the E_1 and $E_1+\Delta_1$ energy gaps. The Raman polarizabilities are denoted by $a_{\rm TO}$ for allowed scattering by TO phonons, $a_{\rm LO}$ for allowed scattering by LO phonons, and a_F for Fröhlich intraband scattering. The selection rules concerning impurity-induced scattering ($a_{\rm FI}$) were calculated using the same expression as for a_F, but shifted by $\hbar\Omega_{\rm LO}/2$ to higher energies. The positive or negative signs of $a_{\rm LO}$ in the interference configurations were derived in a microscopic formulation of DP scattering, which is not presented here.

(001) face: $x=[001]$, $y=[010]$, $z=[001]$, $x'=\frac{1}{\sqrt{2}}[110]$, $y'=\frac{1}{\sqrt{2}}[\bar{1}10]$		
(I)	$\bar{z}(x',x')z$	$\lvert a_F+a_{\rm LO}\rvert^2+\lvert a_{\rm FI}\rvert^2$
(II)	$\bar{z}(y',y')z$	$\lvert a_F-a_{\rm LO}\rvert^2+\lvert a_{\rm FI}\rvert^2$
(III)	$\bar{z}(x,x)z$, $\bar{z}(y,y)z$	$\lvert a_F\rvert^2+\lvert a_{\rm FI}\rvert^2$
(IV)	$\bar{z}(y,x)z$, $\bar{z}(x,y)z$	$\lvert a_{\rm LO}\rvert^2$
(110) face: $x=\frac{1}{\sqrt{2}}[\bar{1}10]$, $y=[001]$, $z=\frac{1}{\sqrt{2}}[110]$		
	$\bar{z}(x,x)z$	$\frac{9}{16}\lvert a_F\rvert^2+\frac{9}{16}\lvert a_{\rm FI}\rvert^2+\lvert a_{\rm TO}\rvert^2$
	$\bar{z}(y,y)z$	$\lvert a_F\rvert^2+\lvert a_{\rm FI}\rvert^2$
	$\bar{z}(y,x)z$, $\bar{z}(x,y)z$	$\lvert a_{\rm TO}\rvert^2$
(111) face: $x=\frac{1}{\sqrt{6}}[11\bar{2}]$, $y=\frac{1}{\sqrt{2}}[\bar{1}10]$, $z=\frac{1}{\sqrt{3}}[111]$		
	$\bar{z}(x,x)z$, $\bar{z}(y,y)z$	$\lvert\frac{5}{6}a_F-\frac{1}{\sqrt{3}}a_{\rm LO}\rvert^2+\frac{25}{36}\lvert a_{\rm FI}\rvert^2+\frac{2}{3}\lvert a_{\rm TO}\rvert^2$
	$\bar{z}(y,x)z$, $\bar{z}(x,y)z$	$\frac{2}{3}\lvert a_{\rm TO}\rvert^2$

V. RESULTS AND DISCUSSION

A. Scattering by LO phonons in HgTe (001)

We studied the resonance behavior of first- and second-order Raman scattering by LO phonons in HgTe (001) in the $\bar{z}(x',x')z$ (I), $\bar{z}(y',y')z$ (II), $\bar{z}(x,x)z$ (III), and $\bar{z}(y,x)z$ (IV) configurations (Table I). The directions of the physically inequivalent axes x' and y' were determined by a detailed x-ray diffraction study[44] of the sample surface.

A typical Raman spectrum of HgTe (001) is shown in Fig. 6, recorded in the $\bar{z}(x,x)z$ geometry at $\hbar\omega_L=2.347$ eV. The 1LO line at 136 cm^{-1},[45] the 2LO scattering at 274 cm^{-1}, and the 3LO process at 410 cm^{-1} are clearly observed. A symmetry-forbidden TO signal was detected at 116 cm^{-1} (Ref. 45). An additional mode at 131 cm^{-1}, in Fig. 6 a weak shoulder, shows a distinct resonant en-

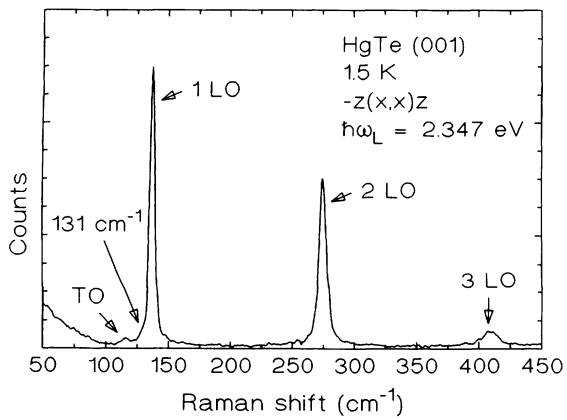

FIG. 6. Raman spectrum of HgTe (001), excited at $\hbar\omega_L=2.347$ eV in the $\bar{z}(x,x)z$ configuration.

hancement near the E_1 and $E_1 + \Delta_1$ gaps in a similar manner as the 1LO process. The origin of this feature, which is more intense in the $\bar{z}(y,x)z$ configuration than in $\bar{z}(x,x)z$ geometry relative to the LO signal, is not clear. However, using Green-function theory Talwar and Vandevyver[46] showed that Te atoms occupying Hg sites in HgTe are able to produce a Raman-active phonon at about 131 cm^{-1} with only small changes in the nearest neighbor force constant (less than 15%).

In Figs. 7(a)–7(d) the resonance behavior of the 1LO scattering efficiencies in the configurations I–IV is displayed, expressed in terms of the squared Raman tensors $|\hat{\mathbf{e}}_S \cdot \overleftrightarrow{R} \cdot \hat{\mathbf{e}}_L|^2$ [Eq. (7)]. The error in the experimental data mainly arises from the uncertainty in the Raman polarizability of silicon, which is known only to within 50%.[29] According to Table I, interference effects between allowed and forbidden scattering are observed in configurations I and II, while pure dipole-allowed and dipole-forbidden scattering is expected in configurations III and IV, respectively.

Comparing Figs. 7(a) and 7(b) with Fig. 7(c), the interference in the $\bar{z}(x',x')z$ geometry is found to be destructive near the E_1 gap and constructive near the $E_1 + \Delta_1$ gap. In the $\bar{z}(y',y')z$ configuration the interference is constructive in the vicinity of the E_1 gap and destructive in the neighborhood of the $E_1 + \Delta_1$ gap. The interference behavior is compatible with the theory described in Sec. IV C including the signs of the deformation potentials $d^5_{1,o}$ and $d^5_{3,o}$. However, in contrast to the calculated resonance profile the Raman efficiency near the $E_1 + \Delta_1$ gap is higher in the $\bar{z}(y',y')z$ configuration than in the $\bar{z}(x,x)z$ geometry. The squared Raman polarizability of dipole-allowed scattering [Fig. 7(d)] near the resonance maxima is about one order of magnitude lower than in the case of forbidden scattering [Fig. 7(c)].

In order to compare the experimental data with the theory reviewed in Sec. IV, dipole-allowed scattering was represented by a_{DP} according to Eq. (10), where the electro-optic part of a_{LO} was neglected for the present. This additional contribution can be expressed using the Faust-Henry coefficient taken from the ratio of a_{LO} to the corresponding a_{TO} measured in backscattering at a (111) face (Sec. V B). As pointed out in Sec. IV C, the impurity-induced mechanism was represented by $a_F(\omega_L - \Omega_{\mathrm{LO}}/2)$. Following Menéndez *et al.*[3] we introduced a parameter $\varepsilon \leq 1$ expressing the fraction of forbidden scattering which interferes coherently with the allowed scattering. Consequently, the noninterfering part $(1-\varepsilon)$ should be due to impurity-induced scattering. The selection rules of Table I thus can be written as

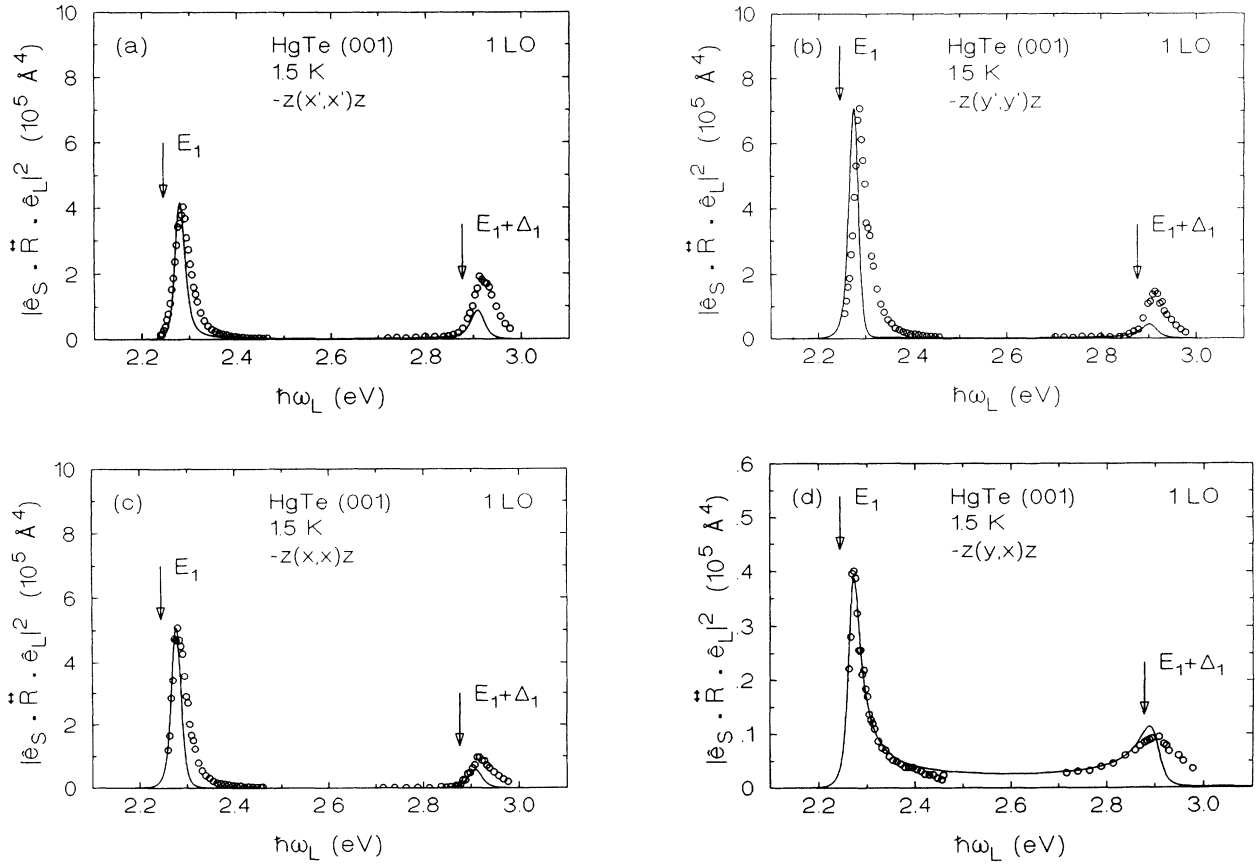

FIG. 7. Squared Raman tensors for 1LO scattering in the vicinity of the E_1 and $E_1 + \Delta_1$ gaps of HgTe (001), observed in the (a) $\bar{z}(x',x')z$, (b) $\bar{z}(y',y')z$, (c) $\bar{z}(x,x)z$, and (d) $\bar{z}(y,x)z$ configurations at 1.5 K. Note the different vertical scale in (d). As in all subsequent figures, the vertical arrows mark the transition energies obtained from the reflectivity measurement. The solid lines represent the best fit to experiment using Eqs. (20).

$$\text{(I)}\quad |\varepsilon^{1/2}a'_F(\omega_L)+a_{\rm LO}(\omega_L)|^2 +(1-\varepsilon)|a'_F(\omega_L-\Omega_{\rm LO}/2)|^2\,, \quad (20a)$$

$$\text{(II)}\quad |\varepsilon^{1/2}a'_F(\omega_L)-a_{\rm LO}(\omega_L)|^2 +(1-\varepsilon)|a'_F(\omega_L-\Omega_{\rm LO}/2)|^2\,, \quad (20b)$$

$$\text{(III)}\quad |\varepsilon^{1/2}a'_F(\omega_L)|^2+(1-\varepsilon)|a'_F(\omega_L-\Omega_{\rm LO}/2)|^2\,, \quad (20c)$$

$$\text{(IV)}\quad |a_{\rm LO}(\omega_L)|^2\,. \quad (20d)$$

The Raman polarizability a'_F differs from Eq. (17) by a real multiplicative factor k fitted to experiment taking into account the surface-field-induced scattering as well as excitonic effects neglected in the derivation of Eq. (17). In the allowed case the excitonic interaction is included by the use of the experimental data of the optical susceptibility when calculating the Raman polarizability $a_{\rm DP}$ [Eq. (10)].

The best fit based on one set of parameters using Eqs. (20) is shown by the solid lines in Figs. 7(a)–7(d). First the $\bar{z}(y,x)z$ configuration [Fig. 7(d)] was fitted treating the deformation potentials $d^5_{1,o}$ and $d^5_{3,o}$, the band-deformation factor ξ [Eq. (11)], and the real constant B [Eq. (10)] as adjustable parameters. The remaining material parameters of HgTe used are listed in Table II. The calculation yields $d^5_{3,o}/d^5_{1,o}=-0.89$, $\xi=2$, and $B=0$. Since dipole-allowed LO scattering in HgTe is distinctly affected by the electro-optic contribution (Sec. V B), no absolute values of the deformation potentials can be derived from this measurement. Nevertheless, a remarkable agreement between experimental data and DP theory is obtained, whereas the differences at the high-energy side of the $E_1+\Delta_1$ gap are probably due to the absorption corrections and the uncertainty in the Raman efficiency of Si in this energy region.[29]

In spite of the good description of the line shape, the fit procedure required the whole resonance curve to be shifted by 24 meV toward the high-energy side with respect to the transition energies obtained from the reflectivity spectrum. Such energy differences between observed resonant Raman peak positions and the ones calculated from the optical constants are a well established phenomenon at the E_1 and $E_1+\Delta_1$ gaps of zinc-blende compounds.[42,49–53] This effect has been investigated in detail by Carles *et al.*[53] in the case of InAs, where the shift between the optical gap and the "Raman gap" was found to depend on the phonon involved but to be temperature independent. However, no theory to account for these experimental observations has been published.[54]

Using the parameters obtained by the fit of the allowed scattering resonance, the squared Raman tensors for the I–III configurations were fitted. The only adjustable parameters were the factors ε and k. The best fit to experimental data was found for $\varepsilon=1$ and $k=4.1$, yielding an excellent agreement of the measured peak maxima with theory near the E_1 gap. In the vicinity of the $E_1+\Delta_1$ gap the experimental values are higher than the calculated ones by a factor 2–3. Whereas the Raman resonance profile of allowed scattering at the E_1 gap is in very good accordance with the lifetime broadening obtained from the optical spectrum (15 meV), the resonance shapes of forbidden scattering [Fig. 7(c)] and the interference configurations [Fig. 7(a) and 7(b)] show a stronger broadening near the critical points. In addition, as observed in the case of InSb (Ref. 3) and GaSb,[4] the resonance profiles recorded in the I–III configurations display an asymmetric behavior on the high-energy sides which is not predicted by theory.

Figure 8 displays the calculated dispersion of $a_{\rm LO}$ and

TABLE II. Material parameters of HgTe, used to calculate the Raman resonance profiles.

$E_1^*=2.269$ eV [a]	$m_{\perp e}=0.123m_0$ [e]
$E_1^*+\Delta_1=2.901$ V [a]	$m_{\perp h1}=0.332m_0$ [e]
$\Gamma_1=0.015$ eV [b]	$m_{\perp h2}=0.470m_0$ [e]
$\Gamma_2=0.025$ eV [b]	$M^*=142166m_0$ [f]
$A^{E_1}=5.639$ eV [b]	$\overline{P}=7.15\times10^{-6}$ eV sm^{-1} [g]
$A^{E_1+\Delta_1}=6.389$ eV [b]	$C_F=1.66\times10^{-6}$ eV m$^{1/2}$ [h]
$\phi_1=1.19$ rad [b]	$C=0.96-i\,0.03$ [i]
$\phi_2=1.23$ rad [b]	$d^5_{1,o}=-19.9$ eV [j]
$\hbar\Omega_{\rm TO}=14.4$ meV [c]	$d^5_{3,o}=14.7$ eV [j]
$\hbar\Omega_{LO}=16.8$ meV [c]	$\xi=2$ [j]
$a_0=6.445$ Å [d]	$f=1/2$ [k]

[a] "Raman gap," from allowed scattering in HgTe (001).
[b] From the line shape analysis of the reflectivity spectrum of HgTe (111).
[c] From the Raman spectra.
[d] Reference 47.
[e] From $\mathbf{k}\cdot\mathbf{p}$ expressions (Ref. 36).
[f] Reference 48.
[g] Reference 26.
[h] Reference 45.
[i] At $\hbar\omega_L=2.60$ eV, from the ratio $a_{\rm LO}/a_{\rm TO}$ (Sec. V B).
[j] For HgTe (111), see Sec. V B.
[k] Reference 37.

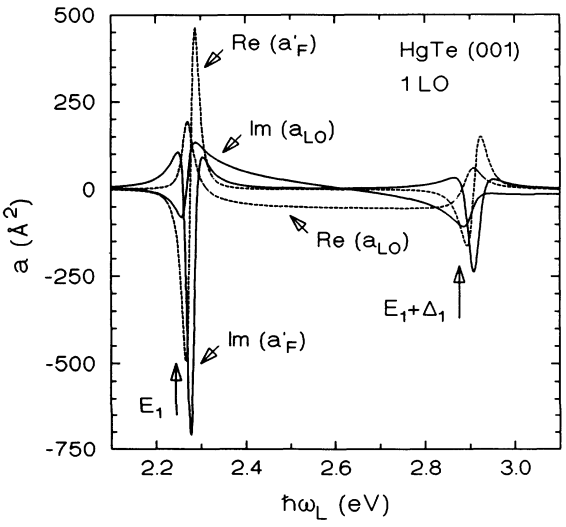

FIG. 8. Calculated dispersion of the Raman polarizabilities $a_{\rm LO}$ of allowed and a'_F of forbidden scattering, used to fit the data in Fig. 7.

a'_F as a function of laser energy. Since $m_{\perp e} - m_{\perp h1(h2)} < 0$, the real part of a'_F is negative at the incoming and positive at the outgoing resonance. Because of the dominance of the imaginary part the two resonances cannot be observed separately. Whereas the components of a'_F have the same sign at E_1 and $E_1+\Delta_1$, the imaginary part of $a_{\rm LO}$ changes its sign between the critical points, leading to a constructive interference at one and a destructive interference at the other critical point, respectively.

The value $\varepsilon = 1$ obtained from the fit implies that the forbidden scattering is caused totally by intrinsic processes: no impurity-induced mechanism is necessary to describe the observed interference behavior. The discussion of this result requires a short review of the theory of impurity states in zero-gap semiconductors, which is a somewhat intricate problem. Impurity levels in these materials occur in the continuous spectra corresponding to either the conduction or the valence band. Therefore, bound states should not exist, but only a certain change in the density of states for energies of the order of the Bohr energy of the impurity state. However, Gel'mont and D'yakonov[55] have pointed out that quasidiscrete acceptor states possibly exist in a semiconductor with zero forbidden gap, provided the hole mass m_h^Γ (at the Γ point) is much larger than the electron mass m_e^Γ, as is the case for HgTe [$m_h^\Gamma = 0.42\,m_0$, $m_e^\Gamma = 0.03\,m_0$ (Ref. 56)]. Therefore acceptors in HgTe are neutral at low temperatures, whereas donors should be ionized at arbitrary temperatures. Thus, the vanishing contribution of the impurity-induced mechanism at 1.5 K on the one hand can be explained if either the acceptor concentration is negligible in Raman scattering or by a thermal freeze-out of acceptor levels found in bulk HgTe at energies of $E_A = 0.7$ meV, 2.25 meV, and 9.5 meV in various transport and magneto-optical investigations.[25,57] Evidence for a temperature dependence in forbidden scattering has been given by measurements on p-doped AlSb.[20] Here the Raman efficiencies obtained at high temperatures were stronger than at low temperatures, an observation that can be explained if ionized impurities are involved in the scattering process. Such a mechanism should be weaker at low temperatures when impurities are frozen out. On the other hand, since donor levels are expected to be ionized even at low temperatures, our result implies that donorlike impurities do not exist in our sample at a concentration high enough to affect the Raman scattering. Recent publications[13,15,21] concerning the scattering at the E_0 and $E_0 + \Delta_0$ gaps of several zinc-blende semiconductors confirm that, at sufficiently low temperatures and with typical impurity concentrations n_i found in *undoped* samples ($n_i < 10^{17}$ cm^{-3}), forbidden scattering can be described very well without taking into account an impurity mechanism. Remarkable agreement between theory and experiment was obtained assuming the discrete and continuous spectra of Mott-Wannier excitons as intermediate states. The impurity mechanism turned out to be not as important as previously[12] assumed.

The scaling factor $k = 4.1$ describes the Raman efficiency of dipole-forbidden scattering to be one order of magnitude stronger in experiment than in theory. An enhancement of the experimentally obtained scattering amplitudes with respect to the theoretical ones has been also observed at the E_1 and $E_1+\Delta_1$ gaps of GaSb and was attributed to the electron-hole correlation in the intermediate states.[4] However, in that case the Raman polarizability of F-induced scattering had to be increased by a factor of 20 in order to fit the measured resonance profiles. Even within the error in the experimental data the effect of the excitonic interaction seems to be less important in HgTe than in GaSb. This fact manifests itself also in the phase angles $\phi_{1,2}$ describing excitonic effects on the optical susceptibilities of Eqs. (3) and (4). Whereas the values $\phi_{1,2} = 1.57$ rad were obtained for GaSb,[4] the corresponding angles in the case of HgTe were found to be $\phi_1 = 1.19$ rad and $\phi_2 = 1.23$ rad. The decreased influence of the excitonic interaction in HgTe may be explained by the relatively large Bohr radius of the 2D exciton[33] due to the high value[45] $\varepsilon_\infty = 15.2$ of the infrared dielectric constant. In addition, the comparatively low value of the scaling factor k points out that surface-field-induced scattering is not important in our sample, as expected for Raman scattering from an undoped semiconductor.[42,53]

Besides the study of interference effects in 1LO scattering, the investigation of 2LO processes can provide information about the significance of the impurity-induced mechanism. Although scattering by two LO phonons is described in fourth-order perturbation theory,[4,50] the Raman efficiency of this process can be comparable to F-induced 1LO scattering since the phonon wave vectors involved are not confined to the center of the BZ in this case. On the other hand, if the impurity-induced mechanism dominates, 1LO scattering is expected to be much stronger than the 2LO process. The 2LO Raman efficiency of HgTe (001) obtained in the $\bar{z}(x,x)z$ configuration is shown in Fig. 9. In the proximity of the E_1 gap the Raman efficiency is lower than the corresponding 1LO maximum (about 20×10^{-5} sr^{-1} cm^{-1}) by a factor of about 0.5. However, this 2LO/1LO ratio is distinctly higher than the value of about 0.01 determined for GaSb at 10 K, where 30% of forbidden 1LO scattering was found to be due to the impurity mechanism.[4] This result thus is another indication of the negligible role of impurity-induced forbidden scattering in HgTe at 1.5 K.

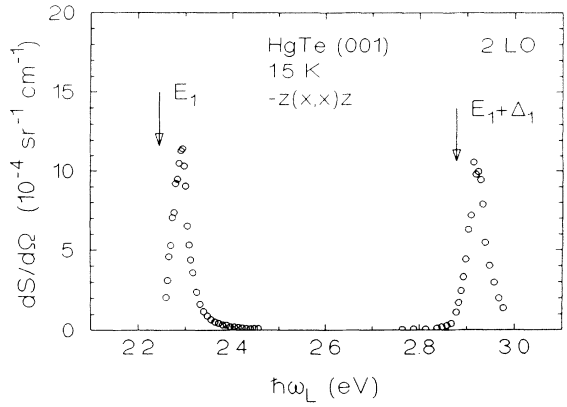

FIG. 9. Experimental Raman efficiency for 2LO scattering in HgTe (001) at 1.5 K in the $\bar{z}(x,x)z$ geometry.

B. Scattering by TO and LO phonons in HgTe (111)

At a (111) surface, in addition to dipole-allowed and dipole-forbidden LO processes, TO scattering can be observed in the $\overline{z}(x,x)z$ geometry (Table I). The resonance behavior of the squared TO Raman tensor in the $\overline{z}(x,x)z$ configuration is displayed in Fig. 10. The solid line shows the best fit to experiment calculated with Eq. (10). The differences between experiment and theory in the proximity of the $E_1 + \Delta_1$ gap are again probably due to the uncertainty in the Raman polarizability of silicon in this energy range.[29] The fit required $B = 0$, $\xi = 2$, $d^5_{3,o}/d^5_{1,o} = -0.74$, and the deformation potentials $d^5_{1,o} = -19.9$ eV and $d^5_{3,o} = 14.7$ eV. The remaining material parameters used were those of Table II. Similar to the case of allowed LO scattering in HgTe (001), the resonance curve had to be shifted by 17 meV to the high-energy side with respect to the transition energies obtained from the optical spectrum. The values determined for the deformation potentials have been confirmed with a deviation of less than 10% by the measurements in the $\overline{z}(y,x)z$ configuration (not shown here), where the same selection rules are valid (Table I).

Since no theoretical calculation exists for the optical deformation potentials in HgTe, we compare our data with the values obtained in Ref. 5 and both experimental and theoretical results for other zinc-blende compounds. Our results are in fair agreement with the deformation potentials, $|d^5_{1,o}| = 24$ eV and $|d^5_{3,o}| = 21.6$ eV, found by Ingale *et al.*[5] via resonant TO scattering in a p-doped HgTe (111) bulk sample at 90 K. We think that our lower value of the three-band deformation potential is reasonable, since due to the lower lifetime broadening at 1.5 K the competing effects of interband coupling and electron damping on the resonance profile of $|a_{\rm TO}|^2$ are suppressed. Our value for $d^5_{1,o}$ lies within the range of calculations which yield values between -10 eV and -20 eV for many tetrahedral semiconductors.[58] In contrast, our results imply a striking deviation in the size of the deformation potential $d^5_{3,o}$ with respect to all other investigated zinc-blende materials. Using nonlocal pseudopotential theory, Pötz and Vogl[58] found for $d^5_{3,o}$ values of about 40 eV in many zinc-blende compounds. Experimentally, Menéndez *et al.*[3] have obtained the deformation potentials $d^5_{1,o} = -16.2 \pm 4$ eV and $d^5_{3,o} = 32.9 \pm 8$ eV for InSb; investigations on GaSb yielded the values $d^5_{1,o} = -10$ eV and $d^5_{3,o} = 60$ eV.[4] As already proposed by Ingale *et al.*,[5] we think that the comparatively small value of the three-band deformation potential in HgTe is a consequence of its inverted band structure: The phonon-induced mixing of the Λ_6 valence band originating from an s-like and the $\Lambda_{4,5}$ valence band arising from a p-like state at the Γ point (as is the case in HgTe) is expected to be smaller than the coupling of two bands both originating from p-like states (as in normal semiconductors).

Using the parameters obtained by the fit of the $\overline{z}(x,x)z$ TO resonance, a comparison of the calculated dispersion of $a_{\rm TO}$ with the corresponding one of $a_{\rm LO}$ [in HgTe (001), Fig. 8] yields the Faust-Henry coefficient of HgTe (Fig. 11). According to Eq. (12) $C = 0.54 - i\,0.04$ at $\hbar\omega_L = 2.25$ eV, $C = 0.93 - i\,0.06$ at $\hbar\omega_L = 2.30$ eV, and $C = 0.96 - i\,0.03$ at $\hbar\omega_L = 2.60$ eV, which reflects that the allowed scattering is weakened by the additional EO contribution. The Faust-Henry coefficient proved to be nearly real below and above the critical points but becomes complex at the E_1 ($C = 0.75 - i\,0.26$ at $\hbar\omega_L = 2.275$ eV) and $E_1 + \Delta_1$ gaps and above $E_1 + \Delta_1$.

No theoretical study is available concerning the Faust-Henry coefficient of HgTe, and therefore we compare our result with values obtained for other zinc-blende compounds. Theoretically, the parameter C was predicted to be negative in many III-V cubic materials, equivalent to an enhancement of allowed scattering by the EO process.[59] This fact has been confirmed experimentally for several of the III-V compounds.[1,2,4] The *ab initio* calculation of Flytzanis[59] also implies that the Faust-Henry coefficient is negative in all II-VI cubic compounds. In contrast, a theoretical study by Kelly[63] predicted a positive Faust-Henry coefficient in ZnS and CdO. In various experiments negative as well as positive values of

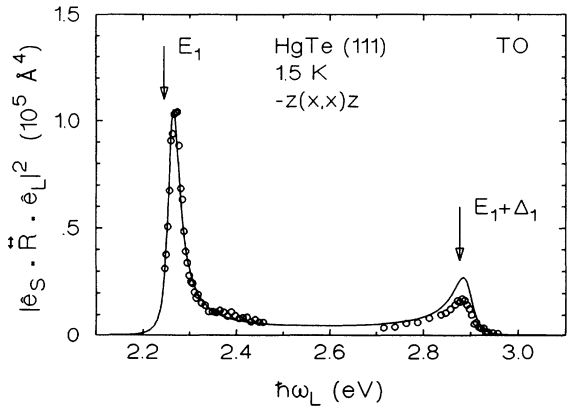

FIG. 10. Squared Raman tensor for scattering by the TO phonon in the vicinity of the E_1 and $E_1 + \Delta_1$ gaps of HgTe (111), observed in the $\overline{z}(x,x)z$ configuration at 1.5 K. The solid line represents the best fit to experiment using Eq. (10).

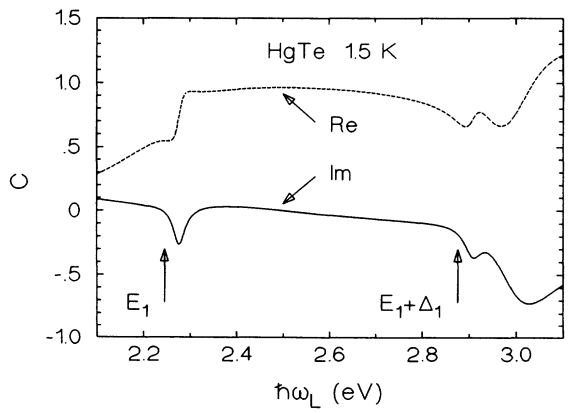

FIG. 11. Faust-Henry coefficient C for HgTe in the energy range of the E_1 and $E_1 + \Delta_1$ gaps at 1.5 K, obtained by a comparison of the calculated dispersion of $a_{\rm LO}$ [HgTe (001)] and $a_{\rm TO}$ [HgTe (111)] using Eq. (12).

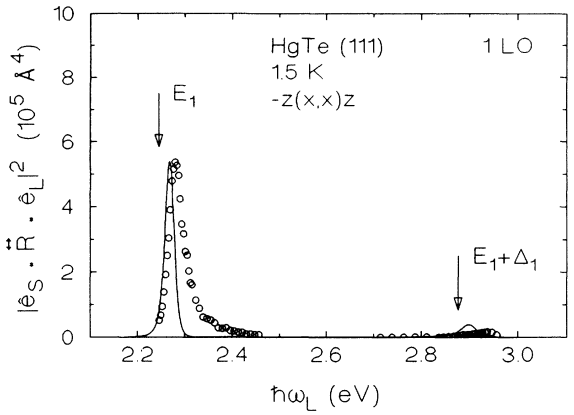

FIG. 12. Squared Raman tensor for scattering by the LO phonon in the vicinity of the E_1 and $E_1 + \Delta_1$ gaps of HgTe (111), observed in the $\bar{z}(x,x)z$ configuration at 1.5 K. The best fit to experiment using Eqs. (10), (12), and (17) is shown by the solid line.

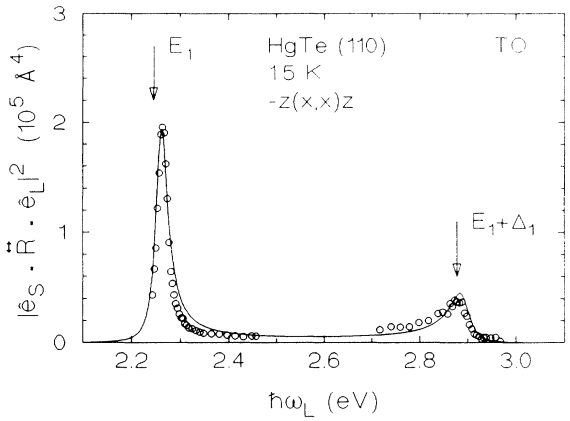

FIG. 13. Squared Raman tensor for scattering by the TO phonon in the vicinity of the E_1 and $E_1 + \Delta_1$ gaps of HgTe (110), observed in the $\bar{z}(x,x)z$ geometry at 1.5 K. The solid line represents the best fit to experiment using Eq. (10).

the coupling constant C were determined in II-VI type crystals.[2,60–62]

Figure 12 displays the squared Raman polarizability of the LO scattering in the $\bar{z}(x,x)z$ geometry. According to Table I, a constructive interference between allowed and forbidden scattering near the E_1 gap and a destructive interference near the $E_1 + \Delta_1$ gap are expected. The latter behavior is clearly observed in Fig. 12. The best fit to the experimental data is shown by the solid line in Fig. 12. Following the results in HgTe (001) only intrinsic (F-induced) forbidden scattering was taken into account, and the parameters obtained for allowed LO scattering in HgTe (001) were used. A scaling factor of $k = 4.6$ is required in order to fit the squared Raman polarizability to the experiment, in good conformity with the result for the (001)-oriented sample. As in the case of HgTe (001) [Fig. 7(b)] the resonance maxima of this interference profile are shifted to higher energies with respect to TO scattering. The asymmetries at the high-energy sides observed in HgTe (001) also appear in the present case.

C. Scattering by TO and LO phonons in HgTe (110)

For backscattering at a (110) face, TO phonon and forbidden LO phonon scattering occur in the $\bar{z}(x,x)z$ geometry (Table I). In the measured spectra (not shown here), a distinct feature below the TO phonon (Raman shift of 116 cm^{-1}) was observed at about 109 cm^{-1}. A mode with nearly the same frequency (108 cm^{-1}) has been found previously in far-infrared[64] and Raman spectra[65] from HgTe and was assigned to an antisite defect in which Hg occupies a Te site. Calculations by Talwar and Vandevyver[46] confirmed that such a configuration can produce a mode at about 105 cm^{-1}.

The resonance shape of the squared TO Raman polarizability measured in $\bar{z}(x,x)z$ geometry is shown in Fig. 13. The solid line displays the best fit to experiment using Eq. (10). The calculation using material parameters of Table II required the following: $B = 0$, $\xi = 2$, $d^5_{3,o}/d^5_{1,o} = -0.59$, and the deformation potentials $d^5_{1,o} = -21.9$ eV and $d^5_{3,o} = 13.0$ eV. This result corroborates the values of the deformation potentials found in HgTe (111). The resonance profile was shifted by 14 meV to the high-energy side with respect to the transition energies obtained in the optical spectrum. A comparison of the differences between the optical gap and the Raman gap observed in the (001)-oriented sample (LO scattering) with the corresponding differences for TO scattering in HgTe (111) and HgTe (110) indicates that the Raman gap depends on the phonon involved in the scattering process.

Figure 14 shows the squared Raman polarizability of the LO phonon in HgTe (110) obtained in the $\bar{z}(x,x)z$ configuration. Only F-induced scattering was taken into account in order to calculate the resonance profile. Using the parameters of Table II and the transition energies from allowed TO scattering, Eq. (17) describes the measured maximum values well if a_F is multiplied by a prefactor $k = 3.1$. However, the positions of the peak max-

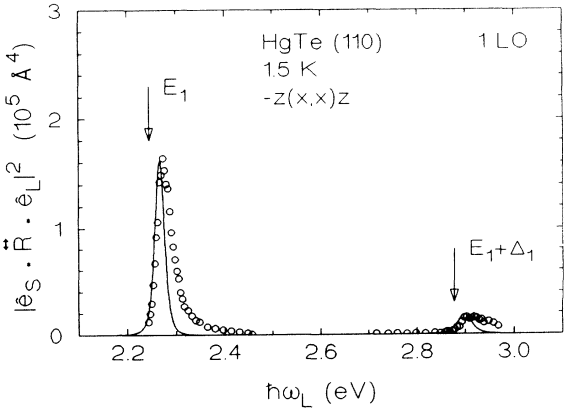

FIG. 14. Squared Raman tensor for scattering by the LO phonon in the vicinity of the E_1 and $E_1 + \Delta_1$ gaps of HgTe (110), observed in the $\bar{z}(x,x)z$ configuration at 1.5 K. The best fit to experiment using Eq. (17) is shown by the solid line.

ima, the broadenings, and the asymmetric behavior at the high-energy sides of the resonance maxima are again not reproduced by theory. A theoretical explanation of these phenomena which were also observable in Raman scattering near the E_1 gap of InSb (Ref. 3) and in the vicinity of the E_1 and $E_1 + \Delta_1$ gaps of GaSb (Ref. 4) is still lacking. Nevertheless, in an energy range where the light penetration depth typically is limited to about 200 Å, different surface effects could modify the Raman resonance shape predicted by theory.

VI. CONCLUSIONS

We have determined the absolute TO and LO phonon Raman scattering efficiencies in HgTe in the energy range of the E_1 and $E_1 + \Delta_1$ band gaps from (001), (110), and (111) surfaces. The values have been compared with a theory for deformation-potential, Fröhlich intraband, and impurity-induced scattering assuming free-electron–hole pairs as intermediate states. However, in the case of the deformation-potential process the effect of excitons was taken into account by using the experimentally obtained shape of the optical susceptibility to calculate the scattering efficiency.

The investigation of interference effects between dipole-allowed and dipole-forbidden LO scattering in HgTe (001) has clearly demonstrated that impurity-induced scattering is negligible in our sample at $T = 1.5$ K. The Raman efficiency of Fröhlich intraband scattering appeared one order of magnitude stronger in experiment than in theory, a fact that can be explained with the electron-hole correlation in the intermediate states.[4]

The optical deformation potentials evaluated from TO scattering in HgTe (111) and HgTe (110) confirmed the results obtained previously by Ingale *et al.*[5] Our values are able to reproduce the TO resonance shape presented in Ref. 5 within the error bars given by the authors when the different lifetime broadenings in both cases are taken into account. By means of the investigation of the interference effects in HgTe (001) the signs of the deformation potentials are also clarified now.

The reduced strength of the DP interband coupling near the E_1 and $E_1 + \Delta_1$ gaps of HgTe with respect to other zinc-blende compounds is probably a consequence of its inverted band structure in the center of the BZ.[5] In contrast to the results reported in Ref. 5, no experimental evidence for three-band contributions to dipole-forbidden scattering was obtained.

The electro-optic contribution was found to reduce intensity of the dipole-allowed scattering by LO phonons, resulting in a positive value of the Faust-Henry coupling coefficient in the energy range under investigation. As prevouisly observed in many III-V compounds, the E_1 and $E_1 + \Delta_1$ band gaps are shifted to higher energies in Raman scattering with respect to the ones obtained from the optical spectrum. This effect still lacks a theoretical explanation.

ACKNOWLEDGMENTS

The authors gratefully acknowledge the help of H. Heinke and F. Goschenhofer for performing x-ray diffractometry and reflectivity measurements, respectively. We are indebted to S. Einfeldt and Y. S. Wu, who grew the samples under investigation. This project has been supported by the Deutsche Forschungsgemeinschaft and the Bundesministerium für Forschung und Technologie.

[1] W. Richter, in *Solid-State Physics*, edited by G. Höhler, Springer Tracts in Modern Physics Vol. 78 (Springer, Berlin, 1976), p. 121, and references therein.
[2] M. Cardona, in *Light Scattering in Solids II*, edited by M. Cardona and G. Güntherodt, Topics in Applied Physics Vol. 50 (Springer, Berlin, 1982), p. 19, and references therein.
[3] J. Menéndez, L. Viña, M. Cardona, and E. Anastassakis, Phys. Rev. B **32**, 3966 (1985).
[4] W. Kauschke, N. Mestres, and M. Cardona, Phys. Rev. B **36**, 7469 (1987).
[5] Alka Ingale, M. L. Bansal, and A. P. Roy, Phys. Rev. B **40**, 12 353 (1989).
[6] P. Vogl, Phys. Rev. B **13**, 694 (1976).
[7] R. M. Martin, Phys. Rev. B **4**, 3676 (1971).
[8] In a strict sense, there also exists an electro-optic contribution to the Raman efficiency of TO phonons, which is expected to be small compared with that of the LO phonons [see, e.g., L. N. Ovander and N. S. Tyu, Phys. Status Solidi B **91**, 763 (1979)].
[9] W. L. Faust and C. H. Henry, Phys. Rev. Lett. **17**, 1265 (1966).
[10] A. Pinczuk and E. Burstein, Phys. Rev. Lett. **21**, 1073 (1968).
[11] A. A. Gogolin and E. I. Rashba, Solid State Commun. **19**, 1077 (1976).
[12] J. Menéndez and M. Cardona, Phys. Rev. B **31**, 3696 (1985).
[13] C. Trallero-Giner, A. Cantarero, M. Cardona, and M. Mora, Phys. Rev. B **45**, 6601 (1992).
[14] W. Kauschke, M. Cardona, and E. Bauser, Phys. Rev. B **35**, 8030 (1987).
[15] A. Cantarero, C. Trallero-Giner, and M. Cardona, Phys. Rev. B **40**, 12 290 (1989).
[16] W. Kauschke and M. Cardona, Phys. Rev. B **35**, 9619 (1987).
[17] W. Kauschke and M. Cardona, Phys. Rev. B **33**, 5473 (1986).
[18] W. Kauschke, V. Vorlíček, and M. Cardona, Solid State Commun. **61**, 487 (1987).
[19] W. Kauschke, V. Vorlíček, and M. Cardona, Phys. Rev. B **36**, 9129 (1987).

[20] V. I. Gavrilenko, D. Martínez, A. Cantarero, M. Cardona, and C. Trallero-Giner, Phys. Rev. B **42**, 11 718 (1990).
[21] C. Trallero-Giner, A. Cantarero, and M. Cardona, Phys. Rev. B **40**, 4030 (1989).
[22] A. Cantarero, C. Trallero-Giner, and M. Cardona, Phys. Rev. B **39**, 8388 (1989).
[23] M. Cardona, in *Solid-State Physics: Advances in Research and Applications*, edited by F. Seitz, D. Turnbull, and H. Ehrenreich (Academic, New York, 1969), Suppl. 11.
[24] L. Viña, C. Umbach, M. Cardona, and L. Vodopyanov, Phys. Rev. B **29**, 6752 (1984).
[25] R. Dornhaus and G. Nimtz, in *Narrow-Gap Semiconductors*, edited by G. Höhler, Springer Tracts in Modern Physics Vol. 98 (Springer, Berlin, 1983), p. 119, and references therein.
[26] S. H. Groves, R. N. Brown, and C. R. Pidgeon, Phys. Rev. **161**, 779 (1967).
[27] E. O. Kane, Phys. Rev. **178**, 1368 (1969).
[28] L. He, C. R. Becker, R. N. Bicknell-Tassius, S. Scholl, and G. Landwehr, J. Appl. Phys. **73**, 3305 (1993).
[29] J. Wagner and M. Cardona, Solid State Commun. **48**, 301 (1983).
[30] D. E. Aspens and A. A. Studna, Phys. Rev. B **27**, 985 (1983).
[31] G. F. Koster, in *Solid-State Physics: Advances in Research and Applications*, edited by F. Seitz and D. Turnbull (Academic, New York, 1957), Vol. 5, p. 173.
[32] Recently, a critical review of this approach has been published by C. C. Kim, J. W. Garland, H. Abad, and P. M. Raccah, Phys. Rev. B **45**, 11 749 (1992).
[33] B. Velický and J. Sak, Phys. Status Solidi **16**, 147 (1966).
[34] W. Hanke and L. J. Sham, Phys. Rev. B **21**, 4656 (1980).
[35] N. Meskini, H. J. Mattausch, and W. Hanke, Solid State Commun. **48**, 807 (1983).
[36] M. Cardona, in *Atomic Structure and Properties of Solids*, Proceedings of the International School of Physics "Enrico Fermi," Course LII, Varenna, 1971, edited by E. Burstein (Academic, New York, 1972), p. 514.
[37] D. J. Chadi, J. P. Walter, M. L. Cohen, Y. Petroff, and M. Balkanski, Phys. Rev. B **5**, 3058 (1972).
[38] A. K. Ganguly and J. L. Birman, Phys. Rev. **162**, 806 (1967).
[39] W. Richter, R. Zeyher, and M. Cardona, Phys. Rev. B **18**, 4312 (1978).
[40] There are two separate intraband deformation potentials corresponding to the conduction band $[d^5_{1,o}(c)]$ and the valence band $[d^5_{1,o}(v)]$, respectively, where optical experiments are sensitive to the difference $d^5_{1,o} = d^5_{1,o}(c) - d^5_{1,o}(v)$. Since $d^5_{1,o}$ varies along [111], only an averaged value is measured in Raman scattering [see, e.g., M. Iliev, M. Sinyukov, and M. Cardona, Phys. Rev. B **16**, 5350 (1977)].
[41] D. C. Hamilton, Phys. Rev. **188**, 1221 (1969).
[42] R. Trommer and M. Cardona, Phys. Rev. B **17**, 1865 (1978).
[43] R. M. Martin, Phys. Rev. B **10**, 2620 (1974).
[44] W. J. Bartels, J. Vac. Sci. Technol. B **1**, 338 (1983).
[45] J. Baars and F. Sorger, Solid State Commun. **10**, 875 (1972).
[46] D. N. Talwar and M. Vandevyver, J. Appl. Phys. **56**, 1601 (1984).
[47] E. Preuss, B. Krahl-Urban, and R. Butz, in *Laue Atlas*, edited by E. A. Niekisch (Bertelsmann, Düsseldorf, 1974).
[48] *CRC Handbook of Chemistry and Physics*, edited by R. C. Weast and M. J. Astle (Chemical Rubber, Boca Raton, 1979).
[49] M. A. Renucci, J. B. Renucci, and M. Cardona, Phys. Status Solidi B **49**, 625 (1972).
[50] M. A. Renucci, J. B. Renucci, R. Zeyher, and M. Cardona, Phys. Rev. B **10**, 4309 (1974).
[51] E. Anastassakis, F. H. Pollak, and G. W. Rubloff, Phys. Rev. B **9**, 551 (1974).
[52] W. Kiefer, W. Richter, and M. Cardona, Phys. Rev. B **12**, 2346 (1975).
[53] R. Carles, N. Saint-Cricq, J. B. Renucci, A. Zwick, and M. A. Renucci, Phys. Rev. B **22**, 6120 (1980).
[54] M. Cardona (private communication).
[55] B. L. Gel'mont and M. I. D'yakonov, Zh. Eksp. Teor. Fiz. **62**, 713 (1972) [Sov. Phys. JETP **35**, 377 (1972)].
[56] K. Shimizu, S. Narita, Y. Nasida, and V. I. Ivanov-Omskii, Solid State Commun. **32**, 327 (1979).
[57] C. Finck, S. Omtezguine, G. Weill, and C. Vérié, in *Proceedings of the Eleventh International Conference on the Physics of Semiconductors, Warsaw, 1972*, edited by M. Miasek (PWN–Polish Scientific, Warsaw, 1972), p. 944.
[58] W. Pötz and P. Vogl, Phys. Rev. B **24**, 2025 (1981).
[59] C. Flytzanis, Phys. Rev. B **6**, 1264 (1972).
[60] R. H. Callender, S. S. Sussman, M. Selders, and R. K. Chang, Phys. Rev. B **7**, 3788 (1973).
[61] J. F. Scott, T. C. Damen, and J. Shah, Opt. Commun. **3**, 384 (1971).
[62] M. Selders, E. Y. Chen, and R. K. Chang, Solid State Commun. **12**, 1057 (1973).
[63] R. L. Kelly, Phys. Rev. **151**, 721 (1966).
[64] M. Grynberg, R. Le Toullec, and M. Balkanski, Phys. Rev. B **9**, 517 (1974).
[65] P. M. Amirtharaj, K. K. Tiong, P. Parayanthal, F. H. Pollak, and J. K. Furdyna, J. Vac. Sci. Technol. A **3**, 226 (1985).